Simulation of random fiber Bragg grating array in polarization-maintaining fiber based on photonic localization effect*

LI Zhihan[1,2], HE Wei[2], and LI Shaode[2]**

1. Key Laboratory of the Ministry of Education for Optoelectronic Measurement Technology and Instrument, Beijing Information Science and Technology University, Beijing 100192, China

2. Beijing Laboratory of Optical Fiber Sensing and System, Beijing Information Science and Technology University, Beijing 100192, China

(Received 13 August 2023; Revised 7 April 2024)

Mid-infrared wavelength switchable and dual-wavelength random laser output has many potential applications. A polarization-maintaining random fiber Bragg grating (PMRFBG) array based on the photonic localization effect of longitudinal invariant transverse disorder in fiber structure is proposed, which can be used as random feedback of dual-wavelength and wavelength switchable output of random fiber laser (RFL). The random fiber Bragg grating (RFBG) array was designed on the panda-type polarization-maintaining fiber (PMF), and the two center wavelengths were 2 151.60 nm and 2 152.22 nm, respectively. The RFBG array was designed on the bow tie-type PMF, and the two center wavelengths were obtained, which were 2 153.08 nm and 2 153.96 nm, respectively. The RFBG array with a center wavelength of 2 139.27 nm was designed on single-mode fiber (SMF). The length of individual fiber Bragg grating (FBG) and PMRFBG, the refractive index modulation depth, the number of cascaded gratings, and the distance between gratings have different effects on the full width at half maximum (*FWHM*) and reflectance of the RFBG and PMRFBG array, but not on the central wavelength, as obtained by simulation using the transmission matrix method. The designed PMRFBG array provides theoretical support for the design of the feedback mechanism of RFL.

Document code: A **Article ID:** 1673-1905(2024)08-0460-12

DOI https://doi.org/10.1007/s11801-024-3164-8

Fiber Bragg grating (FBG) is widely used as optical component[1-3] in the field of fiber laser[4] and fiber optical sensing[5] because of its small size, lightweight, corrosion resistance, high immunity to electromagnetic interference[6], low transfer loss[7], and good wavelength selectivity.

As a new type of fiber laser without a fixed resonant cavity, the random fiber laser (RFL)[8,9] has become a potential light source for communication, sensing, biology, and other fields because of its high efficiency, low cost, and small structure. Conventional RFLs based on Rayleigh scattering[10] to provide feedback to achieve laser output have disadvantages, such as high cost, large overall device, low starting threshold, severe mode competition, and low slope efficiency. Therefore, random fiber Bragg grating (RFBG) is proposed to realize the feedback for the excitation of laser of RFL with short cavity by preparing an array of randomly spaced gratings on the fiber in terms of the photonic localization effect[11,12]. LIZARRAGA et al[13] inscribed randomly spaced Bragg gratings of the same grid length and the same central wavelength with a reflectivity of about 7% to 8% on baited germanium and erbium co-doped single-mode fibers (SMFs), and the random grating arrays formed a composite resonant cavity with a high-quality factor and a gain wavelength range around the central wavelength of the grating. With 980 nm pump light, the laser output exhibits typical laser threshold behavior. ZHANG et al[14] proposed a multi-wavelength narrow-linewidth Brillouin RFL based on RFBG which can offer 25 000 enhancement scatterers on a 2.5-cm-long SMF. The increase of the mode spacing and the improvement of feedback strength by increasing enhancement scatterers can initiate Stokes light of order 14 with the linewidth of less than 1 kHz and the signal-to-noise ratio (*SNR*) up to 41 dB. Furthermore, POPOV et al[15] generated an RFL with a relative intensity noise (RIN) of −110 dB/Hz and a linewidth of 1 kHz with high efficiency (4.5%) as a result of the feedback strength improvement of

* This work has been supported by the National Natural Science Foundation of China (Nos.52105540 and 51975044).

** HE Wei is a professor at the School of Instrument Science and Opto-electronics Engineering, Beijing Information Science and Technology University. He received his Ph.D. degree in 2015 from Hefei University of Technology. His research interests are mainly in fiber optic sensing and fiber laser systems. E-mail: gregg1986@sina.com

RFBG by building a ring-cavity using new writing technology.

Therefore, the role of RFBG as a feedback mechanism for RFL is well recognized. Furthermore, the transfer matrix method and photonic localization theory allow polarization-maintaining FBG (PMFBG) to achieve dual-wavelength excitation by providing feedback for RFL. Here, the design of resonant mid-infrared wavelengths is motivated by the wide applications of mid-infrared wavelength lasers in the military[16] and biomedical[17] fields. So far, although the RFBG based on common SMF and polarization-maintaining fiber (PMF) for mid-infrared wavelength laser output couldn't be technologically realized, their simulations such as the effects of the period, length, modulation depth, and different spacing of individual FBG and PMFBG on RFBG and polarization-maintaining RFBG (PMRFBG) are significant and indispensable.

Since the RFL does not necessarily have a fixed resonant cavity, fiber grating arrays as the feedback unit are prepared on a passive SMF and PMF to achieve stable outputs, respectively, according to photon localization theory and transfer matrix theory. Here, optical characteristics of single-mode RFBG, panda, and bow tie-type PMRFBG are simulated and analyzed.

When photons in a disordered medium propagate, some will escape from the gain medium to as optical loss due to scattering, and some undergo multiple scatterings to form a closed loop in the medium. Light in the medium is confined in a certain volume and cannot continue to propagate anymore and thus would excite random laser as a result of the photon localization effect[10] as shown in Fig.1(d). The strength of the photon localization can be described by a localization parameter bl_t, where b is the equivalent light wave vector in a disordered medium, and l_t is the mean free path of the transport in a disordered medium. The smaller bl_t is, the stronger photon localization is. Only when the length of RFBG is larger than the photon localization length can the effective output of the RFBG laser be guaranteed. The overall transmittance of grating $T(L)$ can be expressed as[18]

$$T(L) \approx \exp(-L/2\xi), \tag{1}$$

where L is the length of RFBG, and ξ is the length of photon localization.

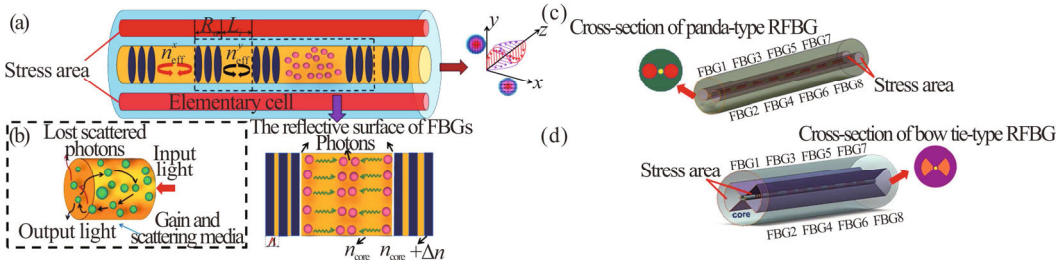

Fig.1 (a) Schematic of the PMRFBG random array; (b) Optical fiber photon localization effect; (c) Panda-type PMRFBG array; (d) Bow tie-type PMRFBG array

A grating fabricated on a PMF can be taken as a Bragg grating fabricated on both its fast and slow axes (referred to as X and Y axes, respectively) due to its unique structure. Its grating period Λ is the same but its effective refractive indices along the X and Y axes are different which are denoted as n_{eff}^x and n_{eff}^y, respectively. Its light propagation is schematically illustrated in Fig.1(a). Light travels slower along the X-axis than the Y-axis. According to the FBG[19] principle, the central wavelengths corresponding to the X-axis and Y-axis of PMFBG respectively can be expressed as follows[20]

$$\lambda_B^x = 2\Lambda n_{\text{eff}}^x, \quad \lambda_B^y = 2\Lambda n_{\text{eff}}^y. \tag{2}$$

According to FBG coupling mode theory, the $R(\lambda)$ of light reflected by FBG can be expressed as

$$R(\lambda) = \frac{\sinh^2(W\sqrt{\kappa^2-\zeta^2})}{\cosh^2(W\sqrt{\kappa^2-\zeta^2}) - \dfrac{\zeta^2}{\kappa^2}}, \tag{3}$$

where ζ is the self-coupling coefficient, and κ is the cross-coupling coefficient. ζ and κ are written as

$$\begin{cases} \zeta = \dfrac{2\pi}{\Lambda} - \dfrac{2\pi}{\lambda} n_{\text{eff}} - \dfrac{2\pi}{\lambda}\delta n_{\text{eff}} \\ \kappa = \dfrac{\pi}{\lambda} s\delta n_{\text{eff}} \end{cases}, \tag{4}$$

where s is the refractive index modulated fringe visibility, and δn_{eff} is the effective refractive index modulation.

For PMFBG, the cross-coupling coefficient of the X-axis and Y-axis is the same, while the self-coupling coefficient is different. The self-coupling coefficient can be expressed as follows

$$\begin{cases} \zeta_x = \dfrac{\pi}{\Lambda} - \dfrac{2\pi}{\lambda} n_{\text{eff}}^x - \dfrac{2\pi}{\lambda}\delta n_{\text{eff}} \\ \zeta_y = \dfrac{\pi}{\Lambda} - \dfrac{2\pi}{\lambda} n_{\text{eff}}^y - \dfrac{2\pi}{\lambda}\delta n_{\text{eff}} \\ f = \dfrac{\pi}{\lambda} s\delta n_{\text{eff}} \end{cases}, \tag{5}$$

where ζ_x is the self-coupling coefficient of the X-axis, and ζ_y is the self-coupling coefficient of the Y-axis. By substituting Eqs.(3) and (4), the reflection spectrum can be expressed as follows

$$R(\lambda)=\frac{\sinh^2\left(W\sqrt{\kappa^2-\zeta_x^2}\right)}{\cosh^2\left(W\sqrt{\kappa^2-\zeta_x^2}\right)-\frac{\zeta_x^2}{\kappa^2}}+\frac{\sinh^2\left(W\sqrt{\kappa^2-\zeta_y^2}\right)}{\cosh^2\left(W\sqrt{\kappa^2-\zeta_y^2}\right)-\frac{\zeta_y^2}{\kappa^2}}. \tag{6}$$

The randomly distributed feedback characteristics of the PMFBG array are investigated using the transfer matrix method. Assuming that all gratings in the array have the same length and refractive index, the spacing L_i between the gratings varies randomly.

Consider each grating and the trailing spacer fiber as a basic unit. Assuming that the length of a single grating is R_0, the transmission matrix $\boldsymbol{W}_{\mathrm{g}}$ of the ith grating in the PMRFBG array can be expressed as

$$\boldsymbol{W}_{\mathrm{g}}=\begin{pmatrix}\cosh(\Omega_x R_0)-\mathrm{i}\frac{\zeta_x}{\Omega_x}\sinh(\Omega_x R_0)+\\ \cosh(\Omega_y R_0)-\mathrm{i}\frac{\zeta_y}{\Omega_y}\sinh(\Omega_y R_0)\end{pmatrix} & -\mathrm{i}\frac{\kappa}{\Omega_x}\sinh(\Omega_x R_0)-\mathrm{i}\frac{\kappa}{\Omega_y}\sinh(\Omega_y R_0)\\ \mathrm{i}\frac{\kappa}{\Omega_x}\sinh(\Omega_x R_0)+\mathrm{i}\frac{\kappa}{\Omega_y}\sinh(\Omega_y R_0) & \begin{pmatrix}\cosh(\Omega_x R_0)+\mathrm{i}\frac{\zeta_x}{\Omega_x}\sinh(\Omega_x R_0)+\\ \cosh(\Omega_y R_0)+\mathrm{i}\frac{\zeta_y}{\Omega_y}\sinh(\Omega_y R_0)\end{pmatrix}\end{pmatrix}, \tag{7}$$

where $\Omega_x=\sqrt{\kappa^2-\zeta_x^2}$, and $\Omega_y=\sqrt{\kappa^2-\zeta_y^2}$. When light passes through the spacer fiber of length L_i in the ith unit, only the phase changes, and its transfer matrix is expressed as follows

$$\boldsymbol{Q}_{L_i}=\begin{pmatrix}G & 0\\ 0 & V\end{pmatrix}, \tag{8}$$

where $G=\exp(\mathrm{i}k_xL_i)+\exp(\mathrm{i}k_yL_i)$, $V=\exp(-\mathrm{i}k_xL_i)+\exp(-\mathrm{i}k_yL_i)$, $k_x=\frac{2\pi n_{\mathrm{eff}}^x}{\lambda}$ and $k_y=\frac{2\pi n_{\mathrm{eff}}^y}{\lambda}$ are wave numbers.

The transfer matrix of the unit composed of grating and spacer fiber can be expressed as follows

$$\boldsymbol{N}_i=\boldsymbol{W}_{\mathrm{g}}\boldsymbol{Q}_{L_i}=\begin{pmatrix}\begin{bmatrix}\cosh(\Omega_x R_0)-\mathrm{i}\frac{\zeta_x}{\Omega_x}\sinh(\Omega_x R_0)+\\ \cosh(\Omega_y R_0)-\mathrm{i}\frac{\zeta_y}{\Omega_y}\sinh(\Omega_y R_0)\end{bmatrix}\times & \begin{bmatrix}-\mathrm{i}\frac{k}{\Omega_x}\sinh(\Omega_x R_0)-\mathrm{i}\frac{k}{\Omega_y}\sinh(\Omega_y R_0)\end{bmatrix}\times\\ \left[\exp(\mathrm{i}k_xL_i)+\exp(\mathrm{i}k_yL_i)\right] & \left[\exp(-\mathrm{i}k_xL_i)+\exp(-\mathrm{i}k_yL_i)\right]\\ \begin{bmatrix}\mathrm{i}\frac{k}{\Omega_x}\sinh(\Omega_x R_0)+\mathrm{i}\frac{k}{\Omega_y}\sinh(\Omega_y R_0)\end{bmatrix}\times & \begin{bmatrix}\cosh(\Omega_x R_0)+\mathrm{i}\frac{\zeta_x}{\Omega_x}\sinh(\Omega_x R_0)+\\ \cosh(\Omega_y R_0)+\mathrm{i}\frac{\zeta_y}{\Omega_y}\sinh(\Omega_y R_0)\end{bmatrix}\times\\ \left[\exp(\mathrm{i}k_xL_i)+\exp(\mathrm{i}k_yL_i)\right] & \left[\exp(-\mathrm{i}k_xL_i)+\exp(-\mathrm{i}k_yL_i)\right]\end{pmatrix}. \tag{9}$$

The amplitude reflectance of the unit can be expressed as follows

$$R_i=\frac{[N_i]_{2,1}}{[N_i]_{1,1}}=\frac{\mathrm{i}\frac{\kappa}{\Omega_x}\sinh(\Omega_x R_0)+\mathrm{i}\frac{\kappa}{\Omega_y}\sinh(\Omega_y R_0)}{\cosh(\Omega_x R_0)-\mathrm{i}\frac{\zeta_x}{\Omega_x}\sinh(\Omega_x R_0)+\cosh(\Omega_y R_0)-\mathrm{i}\frac{\zeta_y}{\Omega_y}\sinh(\Omega_y R_0)}. \tag{10}$$

The amplitude transmittance of the unit can be expressed as follows

$$T_i=\frac{1}{[N_i]_{1,1}}=\frac{\exp(\mathrm{i}k_xL_i)+\exp(\mathrm{i}k_yL_i)}{\cosh(\Omega_x R_0)-\mathrm{i}\frac{\zeta_x}{\Omega_x}\sinh(\Omega_x R_0)+\cosh(\Omega_y R_0)-\mathrm{i}\frac{\zeta_y}{\Omega_y}\sinh(\Omega_y R_0)}. \tag{11}$$

The relationship between the transfer matrix of a cell and its amplitude transmittance and reflectance can be expressed as follows

$$\boldsymbol{s}_i=\begin{pmatrix}\frac{1}{t_i^*} & -\frac{r_i^*}{t_i^*}\\ -\frac{r_i}{t_i} & \frac{1}{t_i}\end{pmatrix}. \tag{12}$$

The overall transfer matrix of all Q units can be expressed as follows

$$\boldsymbol{S}_Q = \boldsymbol{s}_1\boldsymbol{s}_2\ldots\boldsymbol{s}_M = \begin{pmatrix} \dfrac{1}{T_M^*} & -\dfrac{R_M^*}{T_M^*} \\ -\dfrac{R_M}{T_M} & \dfrac{1}{T_M} \end{pmatrix}. \tag{13}$$

T_M and R_M are the overall amplitude transmittance and reflectance of the grating array, respectively. The reflectance of light intensity and transmittance of a single unit are denoted as $\rho=|r|^2$ and $\tau=|t|^2$, respectively. The light intensity transmittance and light intensity reflectance of the corresponding array composed of M gratings with the same characteristics are $\tau_M=|T_M|^2$ and $\rho_M=|R_M|^2$, respectively.

When there are enough gratings in the array, the transmittance can be expressed as[21]

$$\lim_{M\to\infty}\frac{1}{M}\ln\tau_M = -\ln\left(\frac{1}{\tau}\right). \tag{14}$$

The cross-section of the designed panda-type PMF is shown in Fig.2(a). The distance between the two stress holes is L_1=52 μm, and the radii of the core and clad are R_{core}=5 μm and R_{clad}=65 μm. The thermal expansion coefficients of the fiber core, cladding, and stress zone are expressed as A=1.07×10^{-6}, B= 5.38×10^{-5}, and C=2.02×10^{-6}, respectively. For unstressed panda-type PMF, the refractive indices of the core and clad are n_{core}=1.458 2 and n_{clad}=1.452 8. The cross-section of the designed bow tie-type PMF is shown in Fig.2(c). The distance between the two stress holes is L_2=13 μm, the radii of the core and clad are R_{core}=5 μm and R_{clad}=65 μm, and the stress zone is formed by subtracting 1/4 circles with radii of 47.5 μm and 6.5 μm, respectively. Other parameters are the same with panda-type PMF.

The influence of stress on the optical properties of PMF is widely acknowledged, rendering PMF highly susceptible to temperature fluctuations[22]. The structural composition of panda-type and bow tie-type PMF differs significantly, with the latter requiring higher temperatures to achieve superior polarization maintenance performance. Therefore, thermal stress distributions of panda-type and bow tie-type PMF cross sections upon ramping up to 1 100 °C and 1 150 °C from room temperature, respectively, are first analyzed, as shown in Fig.3. The change of temperature will cause the uneven distribution of stress in the fiber core, resulting in birefringence, which results in the different effective refractive index of fast axis and slow axis respectively.

By analyzing and solving the electric field mode of panda-type PMF, it can be obtained that $n_{\text{eff}}^x = 1.454\,992$, $n_{\text{eff}}^y = 1.454\,567$, that is, the mode birefringence coefficient is B=4.25×10^{-5}. The mode field distributions are shown in Fig.4(a—d). By analyzing and solving the electric field mode of bow tie-type PMF, it can be obtained that $n_{\text{eff}}^x = 1.456\,162\,2$, $n_{\text{eff}}^y = 1.455\,573\,5$, that is, the mode birefringence coefficient is B=5.887×10^{-5}. The mode field distribution is shown in Fig.4(e—h). As can be seen from Fig.4, random grating arrays are prepared on the two-type PMFs respectively, which can make the light energy extremely locked at the core propagation.

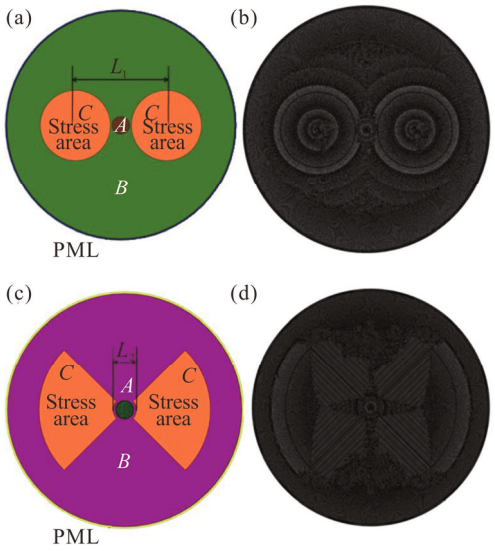

Fig.2 (a) Cross-section of panda-type PMF and (b) its meshing diagram using FEM; (c) Cross-section of bow tie-type PMF and (d) its meshing diagram using FEM

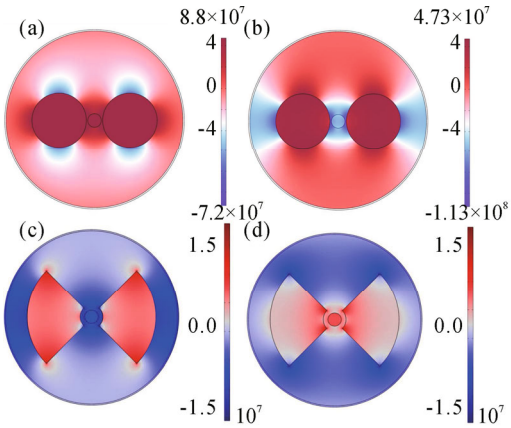

Fig.3 Thermal stress distributions of (a, b) panda-type PMF and (c, d) bow-tie-type PMF cross-sections at (a, b) 1 100 °C and (c, d) 1 150 °C

The lengths, the modulation depths of refractive index, the period, and the random grating spacings of bothpanda- and bow tie-type PMFBGs are taken as 1 mm, 6.5×10^{-5}, 0.739 6 μm, and 4—6 mm, respectively to explore the influences of increasing the number of gratings on the reflection spectrum of the panda-type. For a comparative study, 19 bow tie-type PMFBG cascades were set. In the simulation process, the increase of grating number is based on the previous basis, and the parameters of all gratings are consistent.

As shown in Fig.5(a—e), with the increased number of panda-type PMFBGs, the overall reflectance and feedback

intensity increases, and the reflection peak number increases as well. The reflectance at the central wavelengths along two axes increases almost in the same way, as shown in Fig.5(g) and (i). Since the birefringence coefficient of bow tie-type PMRFBG is higher, the central wavelength difference between the two axes is more obvious at 2 153.08 nm and 2 153.96 nm, respectively, as shown in Fig.5(f). The jump for full width at half maximum (*FWHM*) could be ascribed to the superposition randomness of interference spectra in PMRFBG. It is therefore reasonable to conclude that the bandwidth is narrow or broad depending on a small or large coincidence.

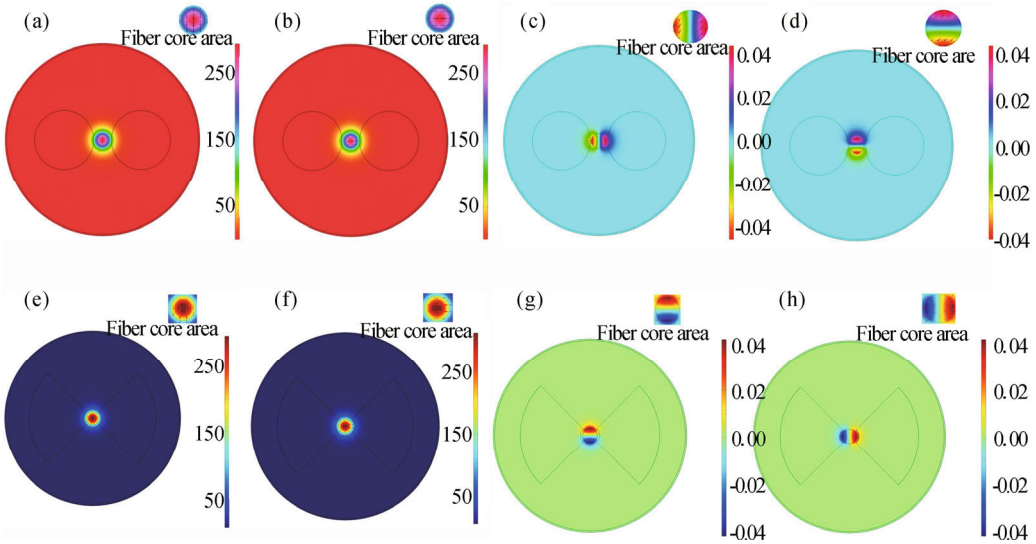

Fig.4 (a, c, e, h) Longitudinal and (b, d, f, g) transverse (a, b, e, f) electric and (c, d, g, h) magnetic field distributions of (a—d) panda-type and (e—h) bow tie-type PMF cross-sections

We can find that a too-large number of gratings would cause a too-high density of reflection peaks for PMRFBG, which therefore deteriorates the output performance of the laser.

By varying the refractive index modulation depths with other parameters taken above, the change of reflection spectrum for panda-type PMRFBG can be investigated as shown in Fig.6(a—e). The modulation depth of bow tie-type PMFBG is 6.5×10^{-5}.

The increase of the modulation depth of single panda-type PMFBG results in the increase of both the overall reflectance and feedback intensities, as revealed in Fig.6 (a—e). Also, Fig.6(h) and (j) show the increase of *FWHM* of reflection peaks along both *X* and *Y* axes with the grating modulation depth. This could be the result of an increased overlap of the increased double-wing satellite peaks around the interference peak.

Through simulation, the overall feedback intensity and density of the reflected spectra of the panda-type PMRFBG were positively correlated with the modulation depths of the refractive index. Considering the threshold of laser output and avoiding feedback saturation, the refractive index modulation depth of a single grating cannot be too low or too high.

Similarly, the modulation depths of single panda-type PMFBG and bow tie-type PMRFBG are set to be 4×10^{-5} and 6.5×10^{-5}, respectively, and the number of cascaded gratings is 19, with the same other parameters above. The effect of single panda-type PMFBG length on its reflection spectrum was investigated as shown in Fig.7. The length of bow tie-type PMFBG is 1 mm.

It can be seen that the increase of single panda-type PMFBG length also increases the overall reflectance and feedback intensity, but almost has no effect on the center wavelength, as shown in Fig.7(a—e). Moreover, the reflectance at the central wavelengths along two axes increases in almost the same way, as revealed in Fig.7(g) and (i). Likewise, since the birefringence coefficient of bow tie-type PMRFBG is superior, the difference in the center wavelength is more obvious, as shown in Fig.7(f). Interestingly, the same grating length results in a greater modulation depth for bow tie-type PMRFBG compared to panda-type PMRFBG, which therefore causes its stronger overall feedback. Fig.7(h) and (j) show that the increase of single panda-type PMRFBG length reduces continuously the *FWHM* along *X* and *Y* axes in a similar way. For a constant period, the longer the grating length is, the smaller the *FWHM* is. Therefore, like a grating number, a single PMFBG length should also be moderate, which will be favorable for optimizing the mode selection performance of PMRFBG, and thus the narrow linewidth laser output.

Assuming that the modulation depth of individual panda-type PMFBG and bow tie-type PMFBG is 6.5×10^{-5}, the length is 1 mm, the period is 0.739 6 μm, and the number of cascaded gratings is 19. The effect of panda-type PMFBG spacing on the reflection spectrum of panda-type PMRFBG was studied. The random interval of bow tie-type PMFBG is 4—7 mm.

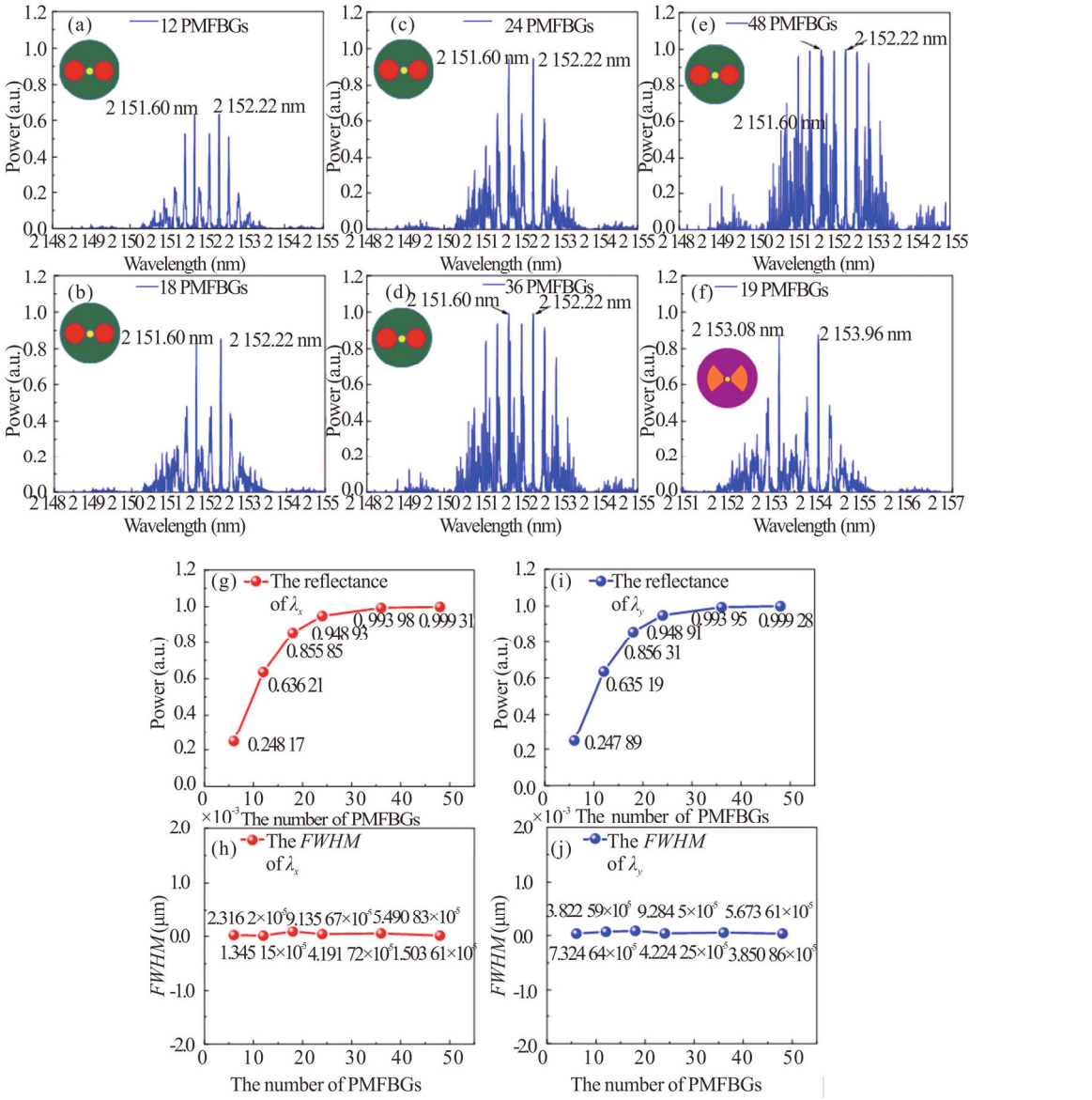

Fig.5 (a—e) Change of the reflection spectrum for panda-type PMRFBG with an increasing number of cascaded gratings; (f) Spectrogram of bow tie-type PMRFBG with 19 gratings; Changes of the reflectance of light at the central wavelengths along (g) *X* and (i) *Y* axes against the increase of cascaded gratings number for panda-type PMRFBG; *FWHMs* of their reflectance maxima along (h) *X* and (j) *Y* axes with the increase of cascaded gratings number

According to the F-P principle, the separation between two neighboring peaks can be written as $\Delta\lambda = \frac{\lambda^2}{2nh}$. Therefore, the increased spacing leads to a narrowed span of the free spectrum, accompanied by densifying and sharpening of reflection peaks, as can be seen in-Fig.8(a—e). The peaks coherently interfered in terms of the F-P mechanism would be further superimposed to form more interference peaks. However, the reflectances along the *X* and *Y* axes remain unchanged, as shown in Fig.8(g) and (i). Since the birefringence coefficient of bow tie-type PMRFBG is superior, the difference in he center wavelength is more obvious, as shown in Fig.8(f). As shown in Fig.8(h) and (j), with the increase of the panda-type PMRFBG spacing, the t *FWHM* of the *X* and *Y* axes finally showed a decreasing trend, and the floating changes of the two were relatively small. In the actual design process, a smaller *FWHM* can be obtained by increasing the integer spacing appropriately.

In order to compare with PMF, the random grating is also prepared on common SMF, as shown in Fig.9. Five gratings with a reflectance of 3% were separated at a random interval of 4—6 mm, and the calculated spatial intensity distribution was consistent with the theoretical study, as shown in Fig.9(b).

Assuming that the length of a single FBG is 1 mm, the refractive index modulation depth is 6.5×10^{-5}, the effective refractive index n_{eff} is 1.446 234, the period is

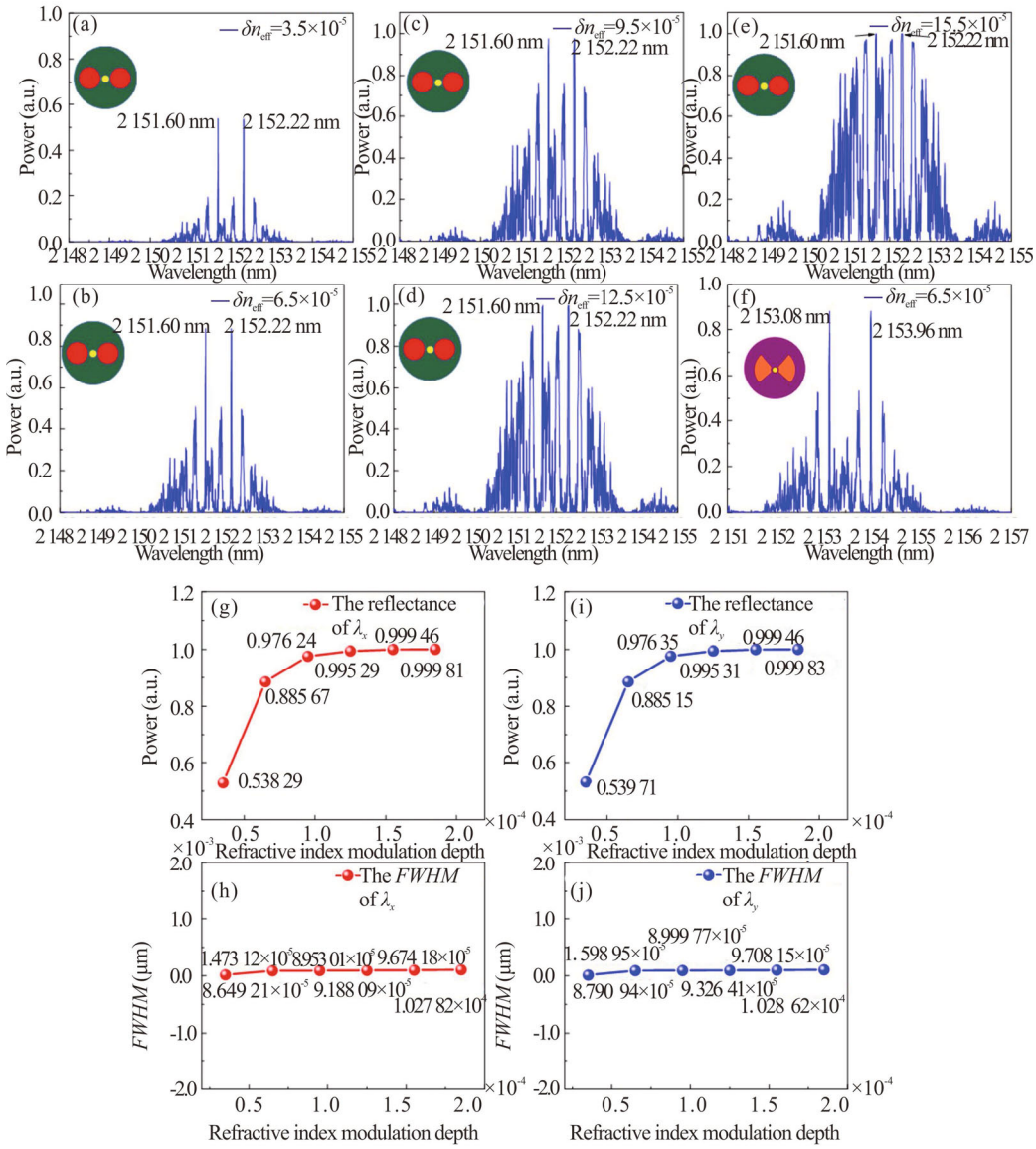

Fig.6 (a—e) Change of the reflection spectrum for panda-type PMRFBG with increasing modulation depths of refractive index; (f) Spectrogram of bow tie-type PMRFBG with modulation depths of refractive index at 6.5×10^{-5}; Changes of the reflectance of light at the central wavelengths along (g) *X* and (i) *Y* axes against the increase of refractive index modulation depths for panda-type PMRFBG; *FWHMs* of their reflectance maxima along (h) *X* and (j) *Y* axes with the increase of refractive index modulation depths

0.739 6 μm, and the grating spacing is randomly selected at 4—6 mm to explore the influence of the different number of FBGs on the RFBG reflection spectrum.

As shown in Fig.10(a—f), with the increase in the number of cascaded gratings, the overall reflectance, and the overall feedback intensity increase, and the density of the reflection peak increases. The reflectance of the central wavelength increases with the number of cascaded gratings. When the number of gratings reaches 48, the central wavelength reflectance approaches 100% as shown in Fig.10(g). Because of the randomness of interference, the increase or decrease of *FWHM* of RFBG is uncertain, as shown in Fig.10(h).

Assuming that the length of a single FBG is 1 mm, the number of cascaded gratings is 19, the effective refractive index n_{eff} is 1.446 234, the period is 0.739 6 μm, and the grating spacing is randomly selected at 4—6 mm. The effect of the refractive index modulation depth of a single FBG on the RFBG grating reflection spectrum was investigated.

As shown in Fig.11(a—f), with the increase of the modulation depth of a single FBG, the overall reflectance and the overall feedback intensity increase. When the modulation depth is 30.5×10^{-5}, band-pass spectra appear, and the mode competition becomes very serious, which is not suitable for the single longitudinal mode output of the laser. Therefore, the modulation depth of a single FBG should not be too

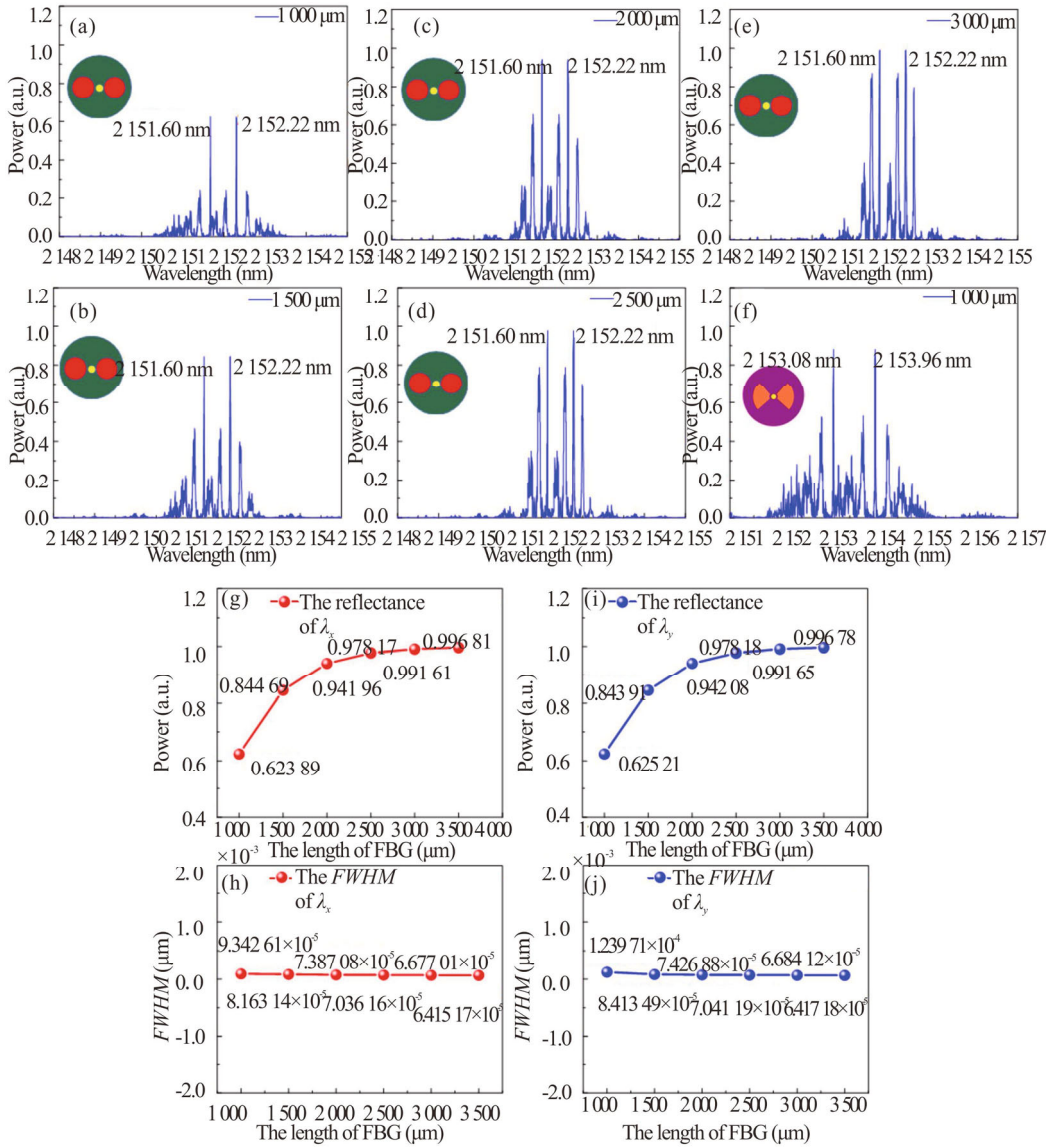

Fig.7 (a—e) Change of the reflection spectrum for panda-type PMRFBG with an increasing length of individual grating; (f) Bow-tie PMRFBG spectrum with a single grating length of 1 mm; Changes of the reflectance of light at the central wavelengths along (g) *X* and (i) *Y* axes against the increase of grating length for panda-type PMRFBG; *FWHMs* of their reflectance maxima along (h) *X* and (j) *Y* axes with the increase of grating length

large. The variation of the reflectance of the resonant wavelength is shown in Fig.10(g). *FWHM* gradually increases with the increase of modulation depth, as shown in Fig.10(h).

Assuming that the modulation depth of a single FBG is 6.5×10^{-5}, the number of cascaded gratings is 19, the effective refractive index n_{eff} is 1.446 234, the period is 0.739 6 μm, and the random interval of gratings is 4—6 mm. The effect of the length of a single FBG on the RFBG grating reflection spectrum was investigated.

As shown in Fig.12(a—f), with the increase in the length of gratings, both the total reflectance and the total feedback intensity increase, and the density of the reflection peak also increases. The *FWHM* decreases with the increase of grating length, which is the same as that of single grating *FWHM*, as shown in Fig.12(h). The length of the grating has no effect on the center wavelength of the grating.

Assuming that the modulation depth of a single FBG is 6.5×10^{-5}, the length of a single FBG is 1 mm, the effective refractive index n_{eff} is 1.446 234, the period is 0.739 6 μm, and the number of cascaded gratings is 19. The effect of grating spacing on the reflection spectrum of RFBG was studied.

It can be seen from Fig.13(a—f) that with the increase of grating spacing, the density of reflection peaks is increasing and the number of reflection peaks is increasing, which conforms to the interference principle of the F-P cavity. As shown in Fig.13(g), the increase in the spacing has no significant effect on the reflectance of the grating. The *FWHM* of resonant wavelength decreases overall, but fluctuates up and down due to the occurrence of

interference, as shown in Fig.13(h). The linewidth can be narrowed by increasing the spacing appropriately. The proposed RFBG and PMRFBG are compared with previous relevant reports, as shown in Tab.1.

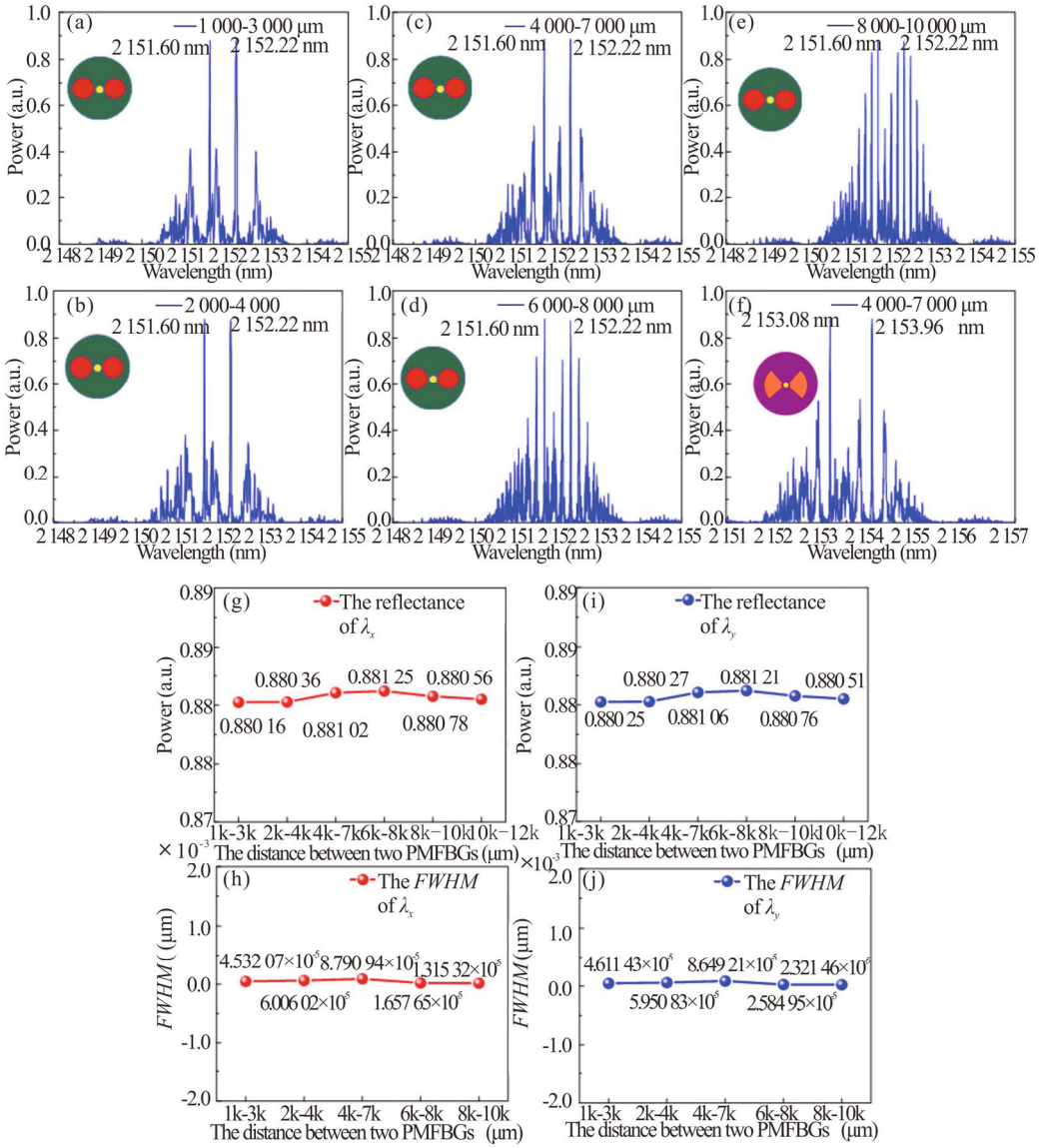

Fig.8 (a—e) Change of the reflection spectrum for panda-type PMRFBG with increasing grating spacing; (f) Bow-tie PMRFBG spectrum with grating spacing of 4—7 mm; Changes of the reflectance of light at the central wavelengths along (g) *X* and (i) *Y* axes against the increase of grating spacing for panda-type PMRFBG; *FWHMs* of their reflectance maxima along (h) *X* and (j) *Y* axes with the increase of grating spacing

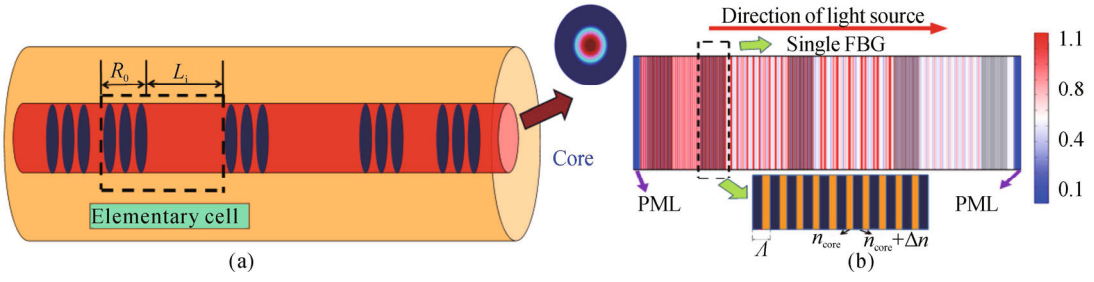

Fig.9 (a) Schematic diagram of single-mode RFBG array; (b) Calculated spatial intensity distribution inside RFBG

In conclusion, the overall feedback intensity and density of the reflected spectra of the panda-type PMRFBG and RFBG were positively correlated with the number of cascaded gratings, the depth of modulation, and the length of the individual grating. Grating spacing is positively correlated with reflectance spectral density but has

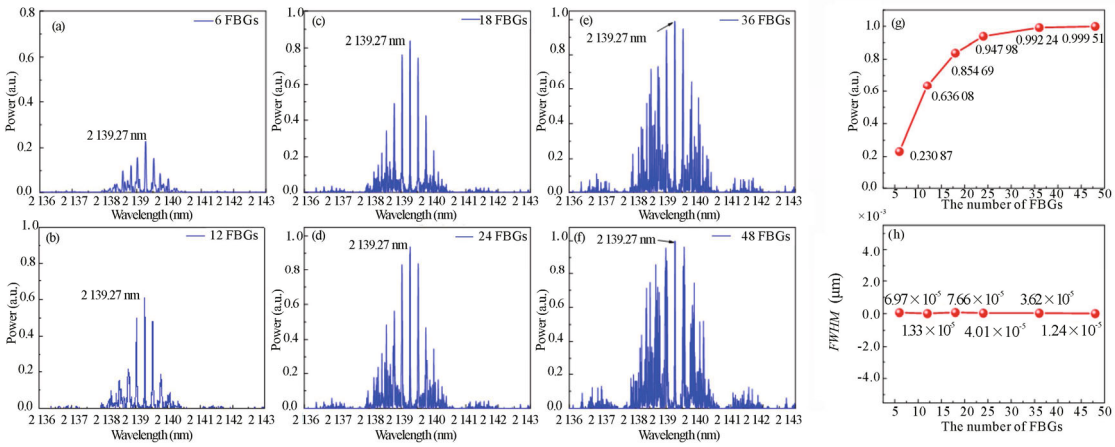

Fig.10 (a—f) Variation of the reflection spectrum of RFBG with an increasing number of cascaded gratings; (g) Reflectance of the RFBG center wavelength changes with the increase of the number of cascaded gratings; (h) *FWHM* of the reflection peak with the largest reflectance in RFBG changes with the increase of the number of cascaded gratings

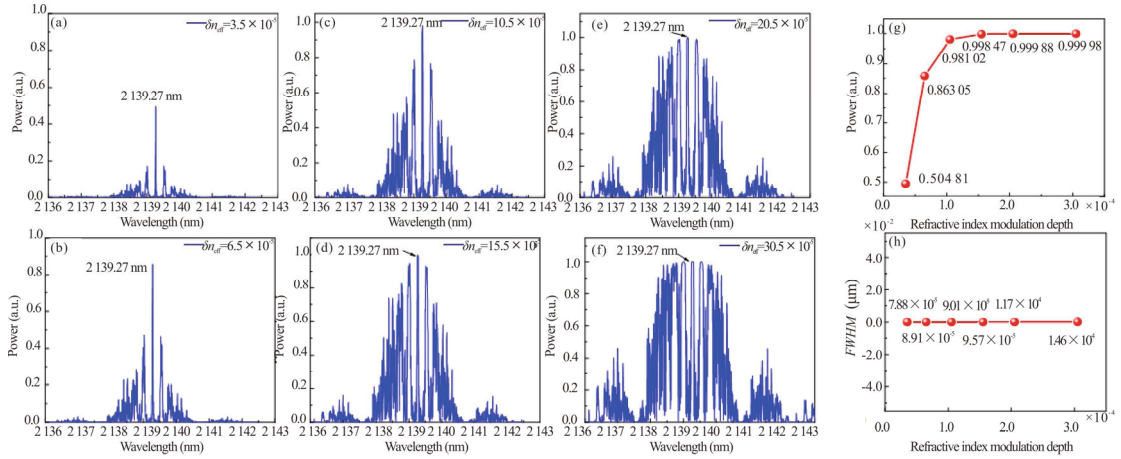

Fig.11 (a—f) Variation of the reflection spectrum of RFBG with increasing modulation depth of individual grating; (g) Reflectance of the central wavelength of RFBG varies with the increase of the modulation depth of individual grating; (h) *FWHM* of the reflection peak with the largest reflectance in RFBG changes with the increase of the grating modulation depth of a single FBG

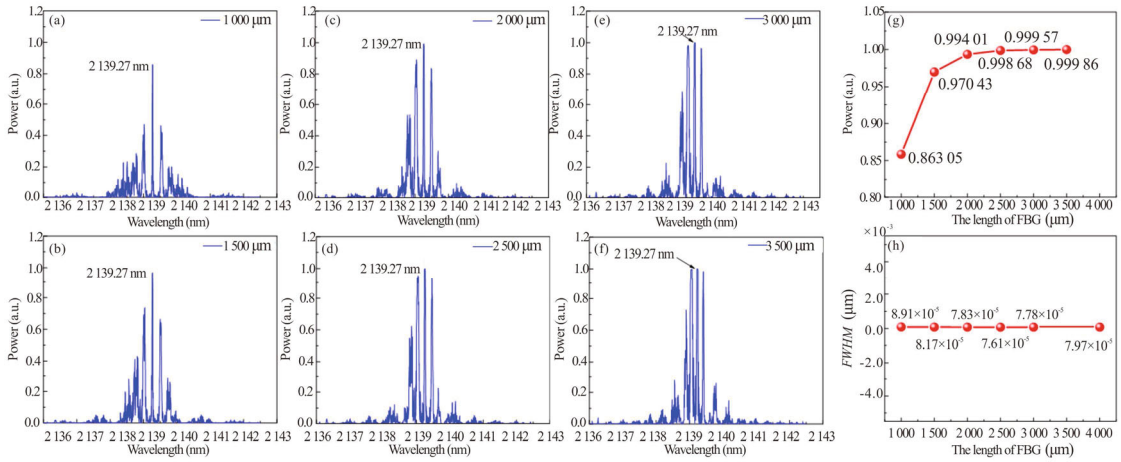

Fig.12 (a—f) Variation of the reflection spectrum of RFBG with the increasing length of the individual grating; (g) Reflectance of the RFBG center wavelength varies with the length of a single grating; (h) *FWHM* of the reflection peak with the largest reflectance in RFBG changes with the increase of the grating length of a single FBG

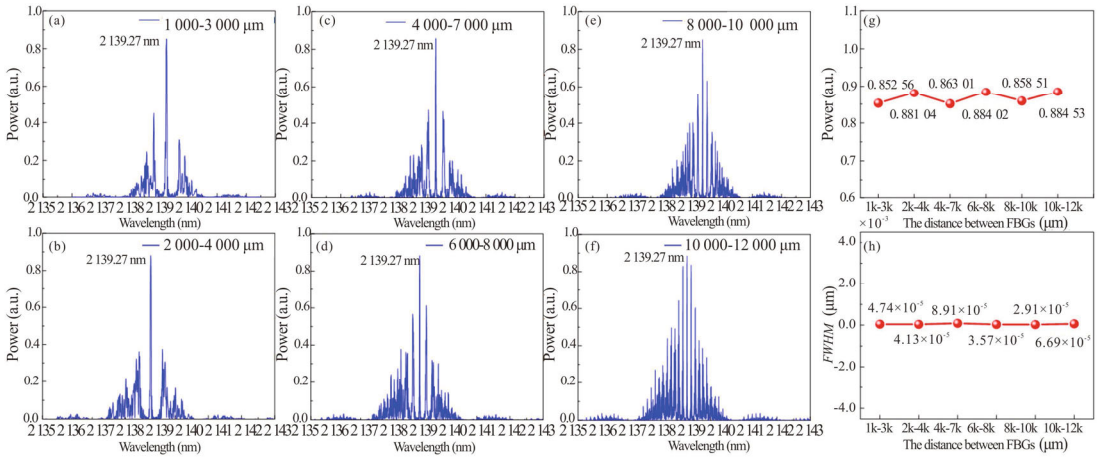

Fig.13 (a—f) Variation of the reflection spectrum of panda-type PMRFBG with increasing grating spacing; (g) Reflectance of RFBG center wavelength changes with the increase of grating spacing; (h) *FWHM* of the reflection peak with the largest reflectance in RFBG changes with the increase of grating spacing

Tab.1 Comparison of parameters between the designed core components and previous related reports

Designer	Core components	Grating number (The number of cascaded gratings)	Grating length (The length of a single grating)	Modulation depth of refractive index (A single grating)	Grating spacing (The distance between two adjacent gratings)
Proposed	Panda type RFBG+bow-tie type RFBG+RFBG	12—24 PMFBGs 6—48 FBGs	1—3 mm PMFBG 1—3.5 mm FBG	3.5×10^{-5}—15.5×10^{-5} PMFBG 3.5×10^{-5}—30.5×10^{-5} FBG	1—10 mm PMFBG 1—1.2 mm FBG
Ref.[23]	RFBG	30 FBGs	3 mm	/	30—80 mm
Ref.[12]	RFBG	20 FBGs	1.19 mm	/	0.2—1.9Π
Ref.[24]	RFBG	2 000 FBGs	0.025 mm	/	0—0.002 5 mm
Ref.[25]	RFBG	15 FBGs	2 mm	/	2—7 mm

essentially no effect on overall feedback intensity. The four parameters also affect the *FWHM* of the panda-tupe PMRFBG and RFBG. The designed PMRFBG array provides theoretical support for the design of dual-wavelength and wavelength switchable output of RFLs based on the random feedback provided by the PMRFBG array.

Ethics declarations

Conflicts of interest

The authors declare no conflict of interest.

References

[1] QIU Z C, SUN R, TENG Y T, et al. Design and test of a low frequency fiber Bragg grating acceleration sensor with double tilted cantilevers[J]. Optics communications, 2022, 507: 127663.

[2] WANG Q Y, TONG X L, ZHANG C, et al. Optical fiber FBG linear sensing systems for the on-line monitoring of airborne high temperature air duct leakage[J]. Chinese physics B, 2022, 31(8): 084204.

[3] SAI Y Z, JIANG M S, SUI Q, et al. FBG sensor array-based-low speed impact localization system on composite plate[J]. Journal of modern optics, 2016, 63(5): 462-467.

[4] LI R F, HU Z J, LI H T, et al. All-fiber laser-self-mixing interferometer with adjustable injection intensity for remote sensing of 40 km[J]. Journal of lightwave technology, 2022, 40(14): 4863-4870.

[5] IP E, FANG J, LI Y W, et al. Distributed fiber sensor network using telecom cables as sensing media: technology advancements and applications[J]. Journal of optical communications and networking, 2022, 14(1): A61-A68.

[6] YU X K, SONG N F, SONG J M. A novel method for simultaneous measurement of temperature and strain based on EFPI/FBG[J]. Optics communications, 2020, 459: 125020.

[7] SAHOTA J K, GUPTA N, DHAWAN D. Fiber Bragg grating sensors for monitoring of physical parameters: a

comprehensive review[J]. Optical engineering, 2020, 59(6): 060901-060901.

[8] ZHANG L, LU P, ZHOU Z, et al. High-efficiency random fiber laser based on strong random fiber grating for MHz ultrasonic sensing[J]. IEEE sensors journal, 2020, 20(11): 5885-5892.

[9] AZMI A N, WAN ISMAIL W Z, ABU HASSAN H, et al. Review of open cavity random lasers as laser-based sensors[J]. ACS sensors, 2022, 7(4): 914-928.

[10] AHMAD H, OOI S I, TIU Z C. 100 GHz free spectral range-tunable multi-wavelength fiber laser using single–multi–single mode fiber interferometer[J]. Applied physics B, 2019, 125: 1-11.

[11] DENG J C, HAN M M, XU Z E, et al. Stable and low-threshold random fiber laser via Anderson localization[J]. Optics express, 2019, 27(9): 12987-12997.

[12] WANG L L, DONG X Y, SHUM P P, et al. Random laser with multiphase-shifted Bragg grating in Er/Yb-codoped fiber[J]. Journal of lightwave technology, 2014, 33(1): 95-99.

[13] LIZÁRRAGA N, PUENTE N P, CHAIKINA E I, et al. Single-mode Er-doped fiber random laser with distributed Bragg grating feedback[J]. Optics express, 2009, 17(2): 395-404.

[14] ZHANG L, XU Y, LU P, et al. Multi-wavelength Brillouin random fiber laser via distributed feedback from a random fiber grating[J]. Journal of lightwave technology, 2018, 36(11): 2122-2128.

[15] POPOV S M, BUTOV O V, BAZAKUTSA A P, et al. Random lasing in a short Er-doped artificial Rayleigh fiber[J]. Results in physics, 2020, 16: 102868.

[16] JI Q, ZONG S, YANG J. Application and development trend of laser technology in military field[C]//ICOSM 2020: Optoelectronic Science and Materials, December 8, 2020, Hefei, China. Washington: SPIE, 2020, 11606: 32-40.

[17] SHIVAKOTI I, KIBRIA G, CEP R, et al. Laser surface texturing for biomedical applications: a review[J]. Coatings, 2021, 11(2): 124.

[18] ABAIE B, MOBINI E, KARBASI S, et al. Random lasing in an Anderson localizing optical fiber[J]. Light: science & applications, 2017, 6(8): e17041-e17041.

[19] HE W, ZHAO J Q, DONG M L, et al. Wavelength-switchable erbium-doped fiber laser incorporating fiber Bragg grating array fabricated by infrared femtosecond laser inscription[J]. Optics & laser technology, 2020, 127: 106026.

[20] LU L D, XU Y J, DONG M L, et al. Birefringent interferometer cascaded with PM-FBG for multi-parameter testing[J]. IEEE sensors journal, 2021, 22(1): 338-343.

[21] IZRAILEV F M, KROKHIN A A, MAKAROV N M. Anomalous localization in low-dimensional systems with correlated disorder[J]. Physics reports, 2012, 512(3): 125-254.

[22] RUFFIN P B. Stress and temperature effects on the performance of polarization-maintaining fibers[C]// Polarimetry: Radar, Infrared, Visible, Ultraviolet, and X-ray, October 1, 1990, Huntsville, AL, USA. Washington: SPIE, 1990, 1317: 324-332.

[23] LV B, ZHANG W, HUANG W, et al. Switchable and compact dual-wavelength random fiber laser based on random Bragg grating array[J]. Optical fiber technology, 2022, 70: 102858.

[24] CHEN C, WANG H Y, LU P, et al. Self-injection locking of a low-noise erbium-doped random fiber laser by a random fiber grating ring[J]. Optics letters, 2023, 48(9): 2389-2392.

[25] HU J, WANG Y F, XING Z K, et al. Stable and ultra-narrow linewidth random fiber laser based on random fiber Bragg gratings[C]//CLEO: QELS_Fundamental Science, May 10-15, 2020, Washington DC, USA. Washington: Optica Publishing Group, 2020: JW2B.4.